Available online at www.sciencedirect.com
ScienceDirect
Optical Materials 29 (2007) 1115–1128
OPTICAL Materials
www.elsevier.com/locate/optmat

Mid-IR transitions of trivalent neodymium in low phonon laser crystals

Yurii V. Orlovskii [a,*], Tasoltan T. Basiev [a], Konstantin K. Pukhov [a], Maxim E. Doroshenko [a], Valery V. Badikov [b], Dmitry V. Badikov [b], Olimkhon K. Alimov [a,c], Marina V. Polyachenkova [a], Leonid N. Dmitruk [a], Vyacheslav V. Osiko [a], Sergey B. Mirov [d]

[a] *Laser Materials and Technologies Research Center, General Physics Institute RAS, 38 Vavilov Street, Bld. D, Moscow 119991, Russia*
[b] *High Technologies Laboratory of Kuban State University, 149 Stavropolskaya Street, Krasnodar 350040, Russia*
[c] *Institute of Nuclear Physics, Uzbekistan Academy of Sciences, Tashkent, Ulugbek 702132, Uzbekistan*
[d] *University of Alabama at Birmingham, 1300 University Boulevard, Birmingham, AL 35294-1170, United States*

Available online 24 July 2006

Abstract

Mid-IR Nd^{3+} transitions perspective for laser oscillation were analyzed in the $CaGa_2S_4$, $PbGa_2S_4$, and $PbCl_2$ crystals and compared with low phonon fluoride crystals. Fluorescence kinetics decay of the high-lying $^4G_{7/2}$ and $^4G_{5/2}$; $^2G_{7/2}$ and low-lying ^4I_J levels and its temperature dependence in the range of 13–295 K were measured. For 5 μm mid-IR transitions of Nd^{3+} the radiative relaxation rates are found to be several times higher and multiphonon relaxation (MR) rates are several times lower in lead and calcium thiogallate crystals compared to low phonon fluoride crystals. MR rate dependence on the Nd^{3+} to the nearest ligand distance R_0 is established experimentally and analyzed in the frame of point-charge model of nonlinear theory of multiphonon relaxation. Mid-IR Nd^{3+} 4–5.5 μm fluorescence spectra of ^4I_i–^4I_j transitions perspective for laser oscillation were measured for the first time in the studied crystals.

PACS: 71.70.Ch; 42.70.Hj

Keywords: Rare-earth doped fluoride; Sulfide and chloride crystals; Mid-infrared laser transitions; Multiphonon relaxation; Nonlinear theory; Radiative transitions

1. Introduction

One of the main problems of the 4–6 μm mid-IR rare-earth (RE) doped laser crystal development is a bypass of radiative transitions by nonradiative ones caused by multiphonon relaxation (MR). This leads to fast excitation decay of the initial laser level and to low fluorescence quantum yield. Hitherto, it was only one theoretically well-proven method to minimize nonradiative losses, namely, to utilize the crystal matrixes with very low phonon spectra. For example, room temperature mid-IR lasing was obtained on Pr^{3+} [1] and Er^{3+} [2] doped chloride laser crystals with very low phonon spectra ($\hbar\omega_{max} \approx 200\ cm^{-1}$) due to the heavy anion. The main reason for the vanishingly small values of multiphonon relaxation rates of mid-IR transitions in these crystals comparing to oxide and fluoride ones is the much larger number of phonons p bridging the energy gap ΔE to the next manifold below. And, it is a well-known fact that an increase of the number of phonons p by one decreases the MR rate by one–two orders of magnitude [3]. Recently mid-IR lasing at 4.3–4.4 μm ($\Delta E = 2300\ cm^{-1}$) of the $^6H_{11/2}$–$^6H_{13/2}$ transition in Dy^{3+} was obtained in calcium ($CaGa_2S_4$) [4] and lead ($PbGa_2S_4$) [5] thiogalate laser crystals with the extent of phonon

* Corresponding author. Tel.: +7 095 1328376; fax: +7 095 1350267.
E-mail address: orlovski@Lst.gpi.ru (Yu.V. Orlovskii).

0925-3467/$ - see front matter © 2006 Elsevier B.V. All rights reserved.
doi:10.1016/j.optmat.2006.05.009

spectra comparable with those for low phonon fluoride crystals like LaF_3 and fluorite-type crystals like SrF_2, CdF_2, BaF_2, and PbF_2. Interestingly, the measured room temperature lifetime of the $^6H_{11/2}$ initial laser level of Dy^{3+} doped $PbGa_2S_4$ is 2 ms [5] and is only 0.3 ms in BaF_2 [6]. However, the maximum phonon frequencies for these crystals are very close. It is 324 cm^{-1} in BaF_2 [7] and even higher in $PbGa_2S_4$. Usually in sulfide crystals the maximum phonon frequency is about 350 cm^{-1}. The scope of this paper is to enlarge the existent data on the measured MR rates of mid-IR transitions in low phonon fluoride, sulfide and chloride RE doped laser crystals to extend our knowledge on multiphonon relaxation and to explain existing experimental results employing advanced nonlinear theory of multiphonon relaxation [8]. Thereto, measurement of multiphonon relaxation rates of Nd^{3+} low-lying $^4I_{15/2}$ level in calcium and lead thiogallate laser crystals are provided using direct laser excitation into the $^4I_{15/2}$ level. The results are compared with the measured MR rates for high-lying $^4G_{7/2}$ and $^4G_{5/2}$; $^2G_{7/2}$ levels of Nd^{3+} in sulfide, chloride, and fluoride crystals.

In Refs. [9–11] it was theoretically predicted and in Refs. [8,12] it was experimentally observed that the MR rates depend strongly on reduced matrix elements of electronic transitions $U^{(k)}$. In this paper it is shown that the MR rates of mid-IR transitions in RE doped crystals with similar phonon spectra (sulfide and fluoride crystals) depend strongly on a rare-earth–ligand distance R_0. So, an increase of R_0 strongly decreases the MR rates for the same transition of specific rare-earth ion in different crystals with close values of maximum phonon frequencies, while an increase of $U^{(k)}$ for different transitions of specific rare-earth ion in one crystal increases the MR rate. This conclusion follows from our studies and it is in a good agreement with nonlinear theory of multiphonon relaxation.

2. Experimental

The $PbCl_2:Nd^{3+}$ (0.2, 0.5, and 0.8 molar%) crystals were synthesized by Laser Materials and Technology Research Center of General Physics Institute RAS. The $PbCl_2$ has an orthorhombic crystal structure with the space-group symmetry Pnma. Lattice parameters of the unit cell are $a = 4.526$ Å, $b = 7.605$ Å and $c = 9.027$ Å. The number of molecules in a unit cell is $z = 4$. The density is 5.94 g/cm^3.

The $PbGa_2S_4:Nd^{3+}$ (0.2 and 0.5 molar%) and $CaGa_2S_4:Nd^{3+}$ (0.16 molar%) crystals were synthesized by High Technologies Laboratory of Kuban State University by modified Bridgman technique in quartz ampoules. The $PbGa_2S_4$ and $CaGa_2S_4$ are biaxial crystals having an orthorhombic crystal structure with a space-group symmetry Fddd. The lattice parameters are $a = 20.706$ Å, $b = 20.380$ Å and $c = 12.156$ Å for $PbGa_2S_4$ and $a = 20.122$ Å, $b = 20.090$ Å and $c = 12.133$ Å for $CaGa_2S_4$. The number of molecules per unit cell is $z = 32$ for both the crystals. The density is 4.92 g/cm^3 for $PbGa_2S_4$ and 3.34 g/cm^3 for $CaGa_2S_4$. The Pb^{2+} or Ca^{2+} ions are partially substituted for Nd^{3+} ions and charge compensation is required during the process of crystal growth. In studied samples the charge compensation of two Nd^{3+} ions is provided by a vacancy and three Pb^{2+} ions and no foreign impurities present in the samples.

Oxygen-free CaF_2:LaF_3 (0.25%):NdF_3 (0.25%) and SrF_2:LaF_3 (1%):NdF_3 (0.2%) crystals with fluorite structure were grown in Laser Materials and Technologies Research Center of General Physics Institute RAS by the Bridgman–Stockbarger technique in a fluorinating atmosphere.

Absorption spectra of the studied crystals were measured using Shimadzu UV-3101 PC UV–VIS–NIR spectrophotometer and FTIR absorption spectrometer.

The fluorescence of the $^4I_{15/2}$ level in $PbGa_2S_4:Nd^{3+}$ (0.2 molar%) and $CaGa_2S_4:Nd^{3+}$ (0.16 molar%) at room temperature was excited by 1.61 μm wavelength obtained after YAP:Nd pump pulsed laser operating at 1.38 μm ($t_p = 40$ ns) and solid-state Raman laser based on barium nitrate crystal with Raman shift of 1047 cm^{-1} ($t_p = 30$ ns) directly into the maximum of absorption spectral line. Fluorescence selection was provided by MDR-23 monochromator (LOMO) with 150 grooves/mm grating. The fluorescence kinetics was detected by a Ge(Au) liquid nitrogen cooled photoresistor with two preamplifiers and digital Tektronix TDS 3032B oscilloscope. A temporal resolution of the whole system was about 10 μs. The fluorescence spectrum for the direct excitation into the $^4I_{15/2}$ manifold was detected using the Tektronix oscilloscope as Boxcar averager under PC program control.

A sum of fluorescence kinetics decay curves of the low-lying $^4I_{15/2}$, $^4I_{13/2}$, and $^4I_{11/2}$ manifolds of Nd^{3+} (see Fig. 1 for energy level diagram) and its temperature dependence in $CaGa_2S_4:Nd^{3+}$, $PbGa_2S_4:Nd^{3+}$, and $PbCl_2:Nd^{3+}$ crystals were measured using 1.56 μm laser excitation into the $^4I_{15/2}$ manifold obtained from the first Stokes of the D_2 Raman shifted 1.06 μm YAG:Nd laser radiation. To separate pump radiation from fluorescence a special filter, transparent for wavelengths longer than 3 μm (I.S.P. Optics, CF-BX-50-76) was used. Fluorescence monitoring was provided by a CdHgTe J15D14 photodetector (EG&G Judson) with an input window made from germanium and transparent for wavelengths longer than 2 μm. The fluorescence signal was amplified by a two stage preamplifier PA-300 with response time of about 2 μs.

The fluorescence kinetics decay curves and the temperature dependencies of the $^4G_{7/2}$ and $^4G_{5/2}$; $^2G_{7/2}$ manifolds of Nd^{3+} in $PbCl_2:Nd^{3+}$, $PbGa_2S_4:Nd^{3+}$, $CaGa_2S_4:Nd^{3+}$ and the $^4G_{5/2}$; $^2G_{7/2}$ manifold in CaF_2:LaF_3 (0.25%):NdF_3 (0.25%) and SrF_2:LaF_3 (1%):NdF_3 (0.2%) crystals were measured by direct excitation using a picosecond laser (EKSPLA) with OPO PG-401 module tunable over the 0.4–2.2 μm spectral range. Resonant fluorescence selection and detection were provided by an ARC-750 spectrometer and a R928 Hamamatsu PMT.

A closed-cycle Janis cryostat with temperature controller was used for cooling of samples below room tempera-

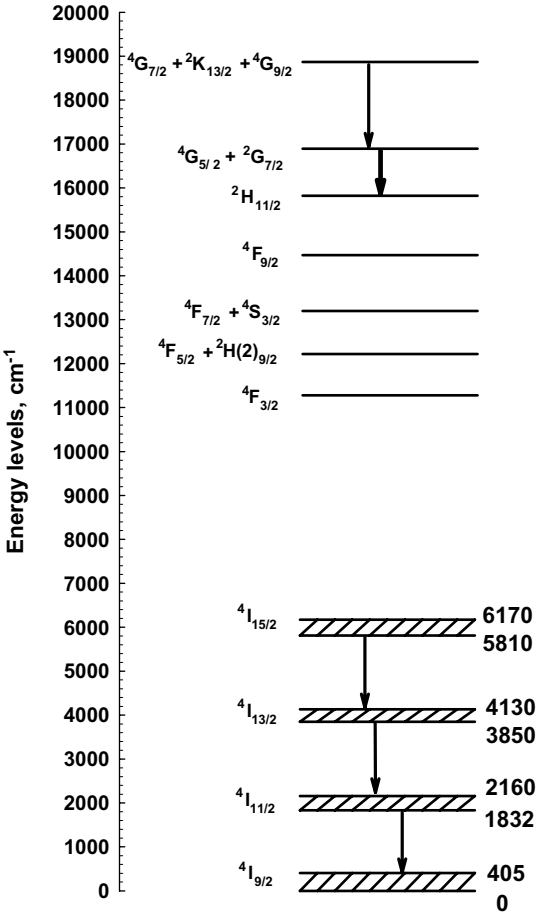

Fig. 1. Energy level diagram of Nd^{3+} ions in the $PbGa_2S_4:Nd^{3+}$ (0.2 molar%) crystal.

ture down to 13 K. Fluorescence kinetics acquisition and recording was provided by a 1 GHz Tektronix TDS 5104 digital oscilloscope.

Also, mid-IR fluorescence spectra of the $CaGa_2S_4:Nd^{3+}$, $PbGa_2S_4:Nd^{3+}$, and $PbCl_2:Nd^{3+}$ crystals were measured using a CW high power (5 W) laser diode array operating at 810 nm and a double grating high throughput SDL monochromator with 100 grooves/mm gratings and 9.6 nm/mm linear reciprocal dispersion. A special filter transparent in the 3.5–6 μm spectral range was used to separate the 4–6 μm fluorescence from an intensive 1.5–3 μm fluorescence observed in higher diffraction orders. The fluorescent signal was detected by a Ge(Au) liquid nitrogen cooled photoresistor. A lock-in amplifier was used to increase the signal to noise ratio. The detected signal was recorded using an ADC and a PC.

3. Nonlinear theory of multiphonon relaxation

In the frame of nonlinear theory of multiphonon relaxation [3,8–13] and for the single phonon frequency model of lattice vibration [14] the p-phonon transition probability $W_{J'\to J}(p)$ between any two J manifolds at $T = 0$ K can be calculated using the following equation written in a form similar to Judd–Ofelt expression for an electro-dipole radiative transition probability between the same manifolds (see below first term of Eq. (14))

$$W_{J'\to J}(p) = \left(\frac{1}{137}\right)^2 (2J'+1)^{-1} 1/\bar{\nu}_{\max} \times \sum_{k=2,4,6} \Xi_k(p) (LSJ\|U^{(k)}\|L'S'J')^2 \eta^p = W_0(p)\eta^p, \tag{1}$$

where $\bar{\nu}_{\max}$ is the maximum phonon frequency of the crystal lattice (in cm^{-1}), $(LSJ\|U^{(k)}\|L'S'J')$ is the reduced matrix element of the unit tensor operator $U^{(k)}$ of rank k that specifies the $J' \to J$ transition within the 4f-electronic configuration (the values of $(LSJ\|U^{(k)}\|L'S'J')^2$ are tabulated [15]). The combined electronic factor Ξ_k(p) accounts for both the point-charge and the exchange-charge interaction between rare-earth ion and the nearest ligands can be presented as

$$\Xi_k(p) = \Xi_k^{\mathrm{pc}}(p) + \Xi_k^{\mathrm{ex}}(p), \tag{2}$$

where $\Xi_k^{\mathrm{pc}}(p)$ is the electronic factor in frame of the point-charge interaction, $\Xi_k^{\mathrm{ex}}(p)$ is the electronic factor in frame of the exchange-charge interaction [13].

In its turn $\Xi_k^{\mathrm{pc}}(p)$ can be expressed as

$$\Xi_k^{\mathrm{pc}}(p) = \frac{cZ}{R_0^2} \begin{pmatrix} l & l & k \\ 0 & 0 & 0 \end{pmatrix}^2 \left[\left(\frac{\langle r^k \rangle}{R_0^k}\right)^2 \frac{(2p+2k)!}{(2k+1)!p!} (2l+1)^2 \left(\frac{q}{e}\right)^2 \right], \tag{3}$$

where c is the velocity of light, Z is the number of anions nearest to the RE ion; R_0 is equilibrium distance between nearest ligand and a RE ion, l is the orbital angular momentum of optical electrons ($l = 3$ for 4f electrons), $\begin{pmatrix} l & l & k \\ 0 & 0 & 0 \end{pmatrix}$ is the 3j-symbol; $\langle r^k \rangle$ is the mean value of the kth power of the radius r of optical 4f-electron, q is the effective charge of the ligand; e is an electron charge.

The phonon factor

$$\eta = \left\langle (\mathbf{u}_{\mathrm{RE}} - \mathbf{u}_{\mathrm{L}})^2 \right\rangle \Big/ 6R_0^2, \tag{4}$$

where $\mathbf{u}_{\mathrm{L}}$ and $\mathbf{u}_{\mathrm{RE}}$ are the ligand and RE ion displacements from their equilibrium positions, respectively, the symbol $\langle \ldots \rangle$ denotes the average over the thermal lattice vibrations. The phonon factor η can be roughly estimated using the following equation [12]:

$$\eta_{\mathrm{est}} = [\langle \mathbf{u}_{\mathrm{cat}}^2 \rangle + \langle \mathbf{u}_{\mathrm{anion}}^2 \rangle]/6R_0^2 \approx \hbar/8\pi c M \bar{\nu}_{\max} R_0^2, \tag{5}$$

where $\hbar$ is Planck's constant, M is the reduced mass of the atoms involved in the vibrations and can be calculated as [12]

$$\frac{1}{M} = \frac{1}{M_{\mathrm{cat}}} + \frac{1}{M_{\mathrm{anion}}}, \tag{6}$$

where M_{cat} = (Ca, Sr, La, Pb, …); M_{anion} = (O, F, S, Cl, …). For the considered crystals the values of η_{est} in the range of 10^{-3}–10^{-4} are expected.

In a single-frequency model of lattice vibration the $W_{MR}(T)$ temperature dependence can be analyzed as [14]

$$W_{MR}(T) = W_{J'\to J}(p)(n(\omega,T)+1)^p, \quad (7)$$

$$n(\omega,T) = (\exp(\hbar\omega_{eff}/kT)-1)^{-1}, \quad (8)$$

where $n(\omega,T)$ is the population of a phonon mode of frequency ω at temperature T described by the Bose–Einstein distribution.

Also, the more realistic (multi-frequency) model of lattice vibration than the single-frequency model can be considered for experimental MR rates analysis [8]. In this case the MR rate between two J-manifolds is given by expression

$$W_{MR}(J'\to J) = \sum_p W_{J'\to J}(p)\bar{\nu}_{max}\rho_p(\Delta E_{J'J})\eta^p, \quad (9)$$

where $\rho_p(\Delta E_{J'J})$ is the convolution of the p functions of $\rho(\Delta E_{J'J})$ (the density of phonon states), which rapidly decreases with a rise of $\Delta E_{J'J}$. All combinations of phonon frequencies make contribution to the p-phonon process are accounted and summation is made for all p.

The neutron scattering data analysis allows to extract the density of phonon states $\rho(\Delta E)$. Unfortunately, at present there are few data about the inelastic neutron scattering by crystals. However, this multi-frequency model was used for the analysis of experimental data on multiphonon relaxation rates at $T = 0$ K in RE doped CaF_2, SrF_2, PbF_2, and BaF_2 crystals [8]. Here and above it is supposed that the crystal-field splitting ($\Delta\varepsilon_{CF}$) of the low-lying J-manifold is small ($\Delta\varepsilon_{CF} \leqslant \hbar\omega_{max}$). The above model resolves the contradiction between the "energy gap" law ($W_{MR}(\Delta E)$) and the dependence of the MR rate on the number of phonons ($W_{MR}(p)$). Now, the energy gap always can be bridged by an integer number of phonons p by taking an appropriate combination of phonon energies within a phonon spectrum of a crystal. But p with maximum contribution can be determined as well.

4. Results and discussion

Absorption spectra of $CaGa_2S_4$:Nd^{3+} (0.16 molar%) and $PbGa_2S_4$:Nd^{3+} (0.2 molar%) crystals in the visible (Fig. 2a) and IR (Fig. 2b) spectral ranges were measured in the single orientation of the crystals. Very strong absorption of the crystal matrix from 500 nm to UV in $CaGa_2S_4$ and from 580 nm to UV in $PbGa_2S_4$ was observed. In the mid-IR spectral range both matrixes are transparent until 8 μm.

The absorption spectra are precisely measured in the $PbGa_2S_4$ crystal with concentration of Nd^{3+} ions 0.5 molar% or $N = 6.25\times10^{19}$ cm^{-3}. The measured absorption spectra are used for calculation of the line-strength of the optical transitions employing Judd–Ofelt theory [16,17].

The experimental integrated absorption cross-sections for the different J–J' transitions are calculated as

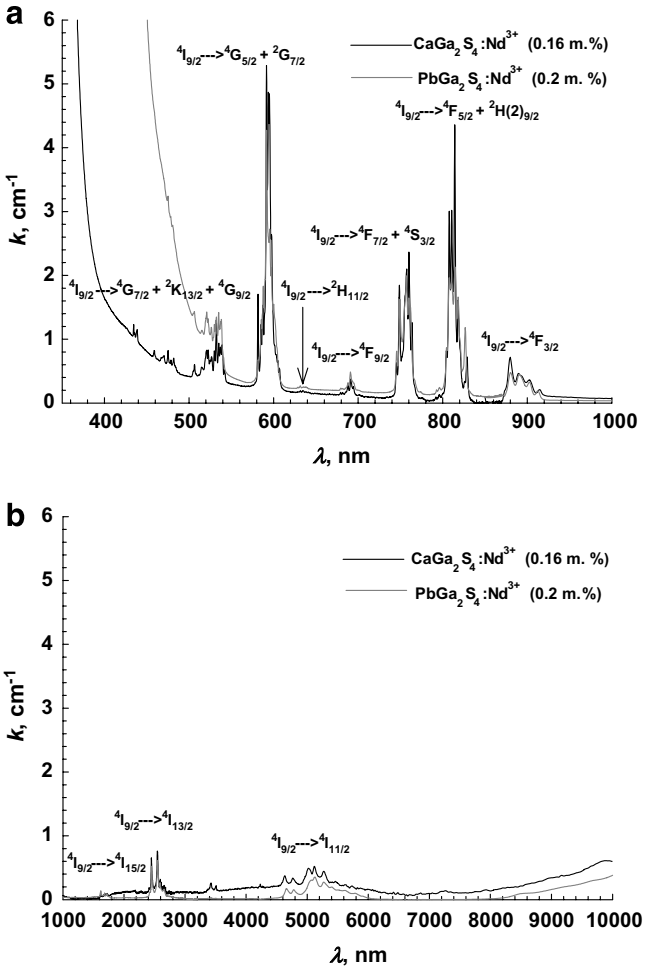

Fig. 2. Absorption spectra in visible and infrared spectral ranges including mid-IR of the $CaGa_2S_4$:Nd^{3+} (0.16 molar%) (black curves) and $PbGa_2S_4$:Nd^{3+} (0.2 molar%) (grey curves) crystals.

$$\sigma_{abs}(J-J') = \int k(\bar{\nu})d\bar{\nu}/N, \quad (10)$$

where k is absorption coefficient in cm^{-1}, $\bar{\nu} = 1/\lambda$ in cm^{-1}.

According to Refs. [18,19] the integrated absorption cross-section of a J–J' optical transition within the ^{4}f shell of a rare-earth ion can be written as

$$\sigma_{abs} = \sigma_{abs}^{ed} + \sigma_{abs}^{md} = \frac{4\pi^2e^2}{3\hbar c}\cdot\frac{\Delta E}{(2J+1)}\cdot\left(\frac{(n^2+2)^2}{9n}\cdot S_{ed} + n\cdot S_{md}\right), \quad (11)$$

where J is the angular momentum of the ground state, ΔE is the transition energy in cm^{-1}, n is a refractive index, S_{ed} is the electric-dipole transition line-strength, and S_{md} is the magnetic-dipole transition line-strength.

In Judd–Ofelt theory [16,17] S_{ed} is expressed as

$$S_{ed} = \sum_{k=2,4,6}\Omega_k\cdot(LSJ\|U^{(k)}\|L'S'J')^2, \quad (12)$$

where Ω_k is the intensity parameter of the theory, S_{md} is expressed as

$$S_{\mathrm{md}} = \frac{\beta^2}{e^2} \cdot (LSJ\|\mathbf{J}+\mathbf{S}\|L'S'J')^2, \tag{13}$$

where β is the Bohr magneton, $(LSJ\|\mathbf{J}+\mathbf{S}\|L'S'J')$ is the reduced matrix elements of operator $\mathbf{J}+\mathbf{S}$. The values are taken from Ref. [19].

It was found that the light beam of the Shimadzu spectrophotometer is polarized along a horizontal orientation of vector **E**. The absorption spectra are measured for two orientations of the sample, one $\mathbf{E}\|c$ (black curve) and the other $\mathbf{E}\perp$c (gray curve). During the measurements the light beam propagated along the *b*-axis of the crystal. For calculation of the integral absorption cross-sections σ_{abs} a spectral background related to the matrix absorption is subtracted (Fig. 3). Then the measured polarized spectra are suitably averaged. Only strong optical transitions with large values of $(LSJ\|U^{(k)}\|L'S'J')^2$ having a decisive influence on the values of electric-dipole line-strengths S_{ed} are used for the calculations (Table 1). For example, the $^4I_{9/2} \rightarrow {}^4G_{5/2} + {}^2G_{7/2}$ transition line-strength has a main contribution from terms with Ω_2 and Ω_4, the $^4I_{9/2} \rightarrow {}^4F_{5/2} + {}^2H(2)_{9/2}$ transition line-strength from Ω_4 and Ω_6, and the $^4I_{9/2} \rightarrow {}^4F_{7/2} + {}^4S_{3/2}$, $^4I_{9/2} \rightarrow {}^4I_{15/2}$, and $^4I_{9/2} \rightarrow {}^4I_{13/2}$ transitions line-strength from Ω_6, only. The following parameters Ω_k were found for $PbGa_2S_4:Nd^{3+}$ by a least squares method, as applied to relevant $\sigma_{\mathrm{abs}}^{\mathrm{ed}}$ obtained from experimentally measured absorption cross-sections σ_{abs} (Table 1): $\Omega_2 = 3.17 \times 10^{-20}$ cm^2, $\Omega_4 = 5.03 \times 10^{-20}$ cm^2, $\Omega_6 = 4.27 \times 10^{-20}$ cm^2.

The radiative relaxation rates for initial levels of mid-IR transitions are calculated as

$$\begin{aligned} A^{JJ'} &= A_{\mathrm{ed}}^{JJ'} + A_{\mathrm{md}}^{JJ'} \\ &= \frac{1}{(2J'+1)} \cdot \frac{32\pi^3 e^2}{3\hbar} \cdot \frac{n(n^2+2)^2}{9} \cdot \Delta E^3 \\ &\quad \cdot \sum_{k=2,4,6} \Omega_k \cdot (LSJ\|U^{(k)}\|L'S'J')^2 + \frac{1}{(2J'+1)} \\ &\quad \cdot \frac{32\pi^3 \cdot n^3}{3\hbar} \cdot \bar{\nu}^3 \cdot \beta^2 \cdot (LSJ\|\mathbf{J}+\mathbf{S}\|L'S'J')^2, \end{aligned} \tag{14}$$

where J' is the angular momentum of the excited state.

Very short radiative decay times for the $^4G_{7/2}$ ($\tau_R = 13.6$ μs); $^4G_{5/2} + {}^2G_{7/2}$ ($\tau_R = 21.2$ μs) and $^4F_{3/2}$ manifolds ($\tau_R = 65.4$ μs) are calculated in $PbGa_2S_4:Nd^{3+}$ (Table 2). The measured decay time ($\tau_R^{\mathrm{meas}} = 60$ μs) of the $^4F_{3/2}$ metastable level (Table 3) is found to be in a good agreement with the calculated one. It should be pointed out that the $^4F_{3/2}$ manifold decay times found in the studied sulfide and chloride crystals are much shorter than those taken from the literature for commonly used laser crystals such as $YAG:Nd^{3+}$ ($\tau = 230$ μs) and $YLF:Nd^{3+}$ ($\tau = 520$ μs). The measured room temperature lifetime of the $^4F_{3/2}$ metastable manifold for $PbGa_2S_4:Nd^{3+}$ ($\tau = 60$ μs) is twice shorter than for $PbCl_2:Nd^{3+}$ ($\tau = 119$ μs) and 1.3 times shorter than for $CaGa_2S_4:Nd^3$ ($\tau = 76$ μs). The main reason is the very high refractive index $n = 2.5$

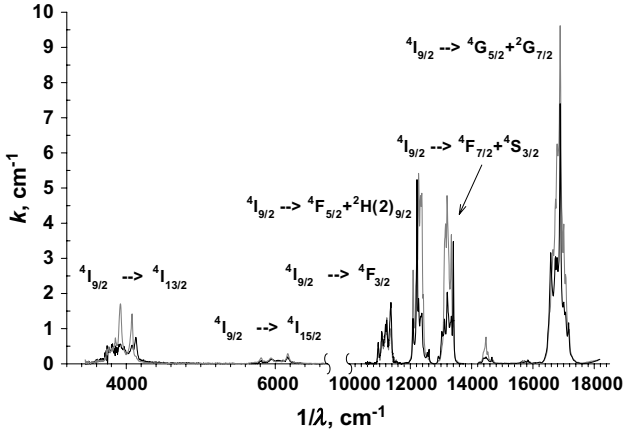

Fig. 3. Polarized absorption spectra of the $PbGa_2S_4:Nd^{3+}$ (0.5 molar%) crystal. Two orientations of the sample: $\mathbf{E}\|c$ (solid black curve) and $\mathbf{E}\perp$c (solid grey curve).

Table 1
Measured absorption cross-sections σ_{abs} in the $PbGa_2S_4:Nd^{3+}$ (0.5 molar%) crystal

Transition	σ_{abs}, 10^{-17} (cm)
$^4I_{9/2} \rightarrow {}^4F_{5/2} + {}^2H(2)_{9/2}$	1.26
$^4I_{9/2} \rightarrow {}^4F_{7/2} + {}^4S_{3/2}$	1.18
$^4I_{9/2} \rightarrow {}^4G_{5/2} + {}^2G_{7/2}$	3.16
$^4I_{9/2} \rightarrow {}^4I_{15/2}$	0.06
$^4I_{9/2} \rightarrow {}^4I_{13/2}$	0.29

Table 2
Calculated radiative rates $\sum A_i$ and radiative lifetimes τ_R of the manifolds in study in the $PbGa_2S_4:Nd^{3+}$ (0.5 molar%) crystal

Manifold	A (s^{-1})	$\tau_R = 1/A$
$^4I_{11/2}$	47.5	21 ms
$^4I_{13/2}$	182	5.5 ms
$^4I_{15/2}$	205	4.9 ms
$^4F_{3/2}$	15,200	65 μs
$^4G_{5/2} + {}^2G_{7/2}$	47,200	21.2 μs
$^4G_{7/2}$	73,500	13.6 μs

Table 3
Measured lifetimes of Nd^{3+} levels in studied crystals

Manifold	$\tau_{\mathrm{meas.}}$, μs (T, K)	$\tau_{\mathrm{meas.}}$ (μs), $T = 295$ K
$PbGa_2S_4$		
$^4G_{7/2}$	12.3 (77 K)	10.5
$^4F_{3/2}$		60
$CaGa_2S_4$		
$^4G_{7/2}$	14.5 (77 K)	13.6
$^4F_{3/2}$	77.5 (18 K)	76
$PbCl_2$		
$^4G_{5/2}$; $^2G_{7/2}$	18.3 (14 K)	5.5
$^4G_{7/2}$	32 (13 K)	23
$^4F_{3/2}$	115 (13 K)	119
$^4I_{11/2}$	11 ms (8 K)	9 ms

for the $PbGa_2S_4$ crystal (see Eq. (14)). The refractive indices in $CaGa_2S_4$ ($n = 2.3$) and in $PbCl_2$ ($n = 2.2$) are also rather high. This leads to increased radiative rates A due to higher photon density of the states and high polarizability of the surrounding medium in comparison with YLF ($n = 1.62$) and YAG ($n = 1.82$).

Let us turn to mid-IR transitions. The fluorescence kinetics of the $^4I_{15/2}$ level in the $PbGa_2S_4$:Nd^{3+} (0.2 molar%) and $CaGa_2S_4$:Nd^{3+} (0.16 molar%) crystals at room temperature measured for selective fluorescence monitoring exhibits exponential decay. But rather weak signal, only one order of magnitude change of fluorescence intensity (curves 2 and 4 in Fig. 4), forced to determine the temperature dependence of the decay time for both the crystals from a fluorescence kinetics of the sum of the cascade mid-IR

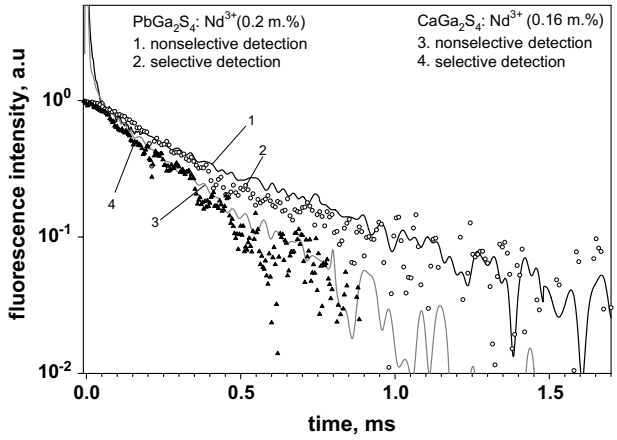

Fig. 4. Comparison of the fluorescence kinetics of the $^4I_{15/2}$ manifold excited at 1.61 μm directly into the maximum of the $^4I_{9/2} \rightarrow {}^4I_{15/2}$ transition and selectively detected at 4.7 μm in the $PbGa_2S_4$:Nd^{3+} (0.2 molar%) and $CaGa_2S_4$:Nd^{3+} (0.16 molar%) crystals at room temperature – curves 2 and 4, and of a sum of fluorescence kinetics of three low-lying ^4I_J manifolds excited at 1.56 μm and detected after optical filter transparent at wavelengths longer than 3 μm – curves 1 and 3.

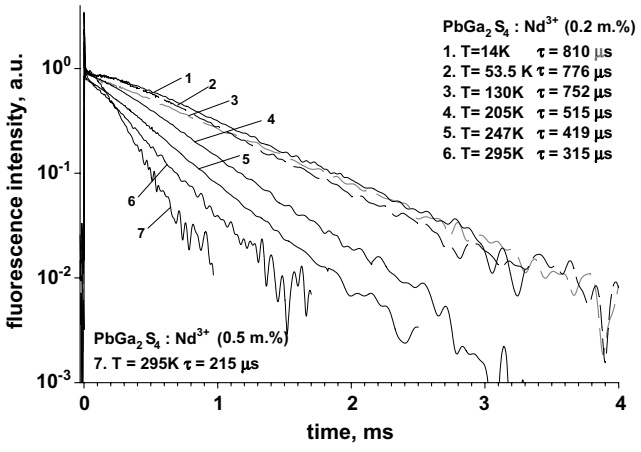

Fig. 5. Temperature and concentration dependencies of a sum of fluorescence kinetics of three low-lying ^4I_J manifolds of the Nd^{3+} ion in $PbGa_2S_4$ under 1.56 μm laser excitation and fluorescence monitoring after optical filter transparent at wavelengths longer than 3 μm.

$^4I_{15/2} \rightarrow {}^4I_{13/2}$; $^4I_{13/2} \rightarrow {}^4I_{11/2}$; and $^4I_{11/2} \rightarrow {}^4I_{9/2}$ transitions at 1.56 μm laser excitation (curves 1 and 3 in Figs. 4, 5 and 8). This allows to acquire not less than two orders of magnitude change of fluorescence intensity with rather large signal-to-noise ratio and to determine the decay time at the long time scale of fluorescence kinetics decay with higher accuracy than in the case of selective fluorescence detection. The measured decay times at the long time scale of fluorescence kinetics decay for both detection methods are found nearly identical for both the crystals at room temperature (Fig. 4). A fast microsecond spike at the very beginning of the sum of fluorescence decay curves could be related to a small fraction of the powerful pump radiation passing through the filters.

Also, we calculated and analyzed solutions of the kinetic rate equations for a four level system with short pulse laser excitation into the highest lying $^4I_{15/2}$ level taking into consideration radiative and multiphonon relaxation processes, only (see Appendix). As a result we found that the measured total fluorescence kinetics at the long time scale is defined by the slowest decay rate among the three cascade fluorescent $^4I_i - {}^4I_j$ transitions. The initial and middle parts of the measured fluorescence decay curve is defined by a sum of decay curves related to all three cascade mid-IR $^4I_{15/2} \rightarrow {}^4I_{13/2}$; $^4I_{13/2} \rightarrow {}^4I_{11/2}$, and $^4I_{11/2} \rightarrow {}^4I_{9/2}$ transitions. Two step excitation as a result of absorption transition from the ground $^4I_{9/2}$ manifold to the excited $^4I_{15/2}$ manifold with the following (during the laser pulse) excited state absorption transition from the $^4I_{15/2}$ manifold to the $^4F_{5/2}$ manifold with subsequent relaxation to the lower-lying levels should be considered as well. With this consideration the measured fluorescence kinetics for a long time scale should be defined also by the slowest decay rate of participated energy levels including the $^4F_{3/2}$ and $^4F_{5/2}$ manifolds. At higher concentrations contribution of the cross-relaxation processes (up- and down conversion) should be taken into account. For example, at room temperature the measured decay time for the long time scale of the total fluorescence kinetics decay in $PbGa_2S_4$:Nd^{3+} (0.5 molar%) crystal is shorter ($\tau = 215$ μs) (curve 7 in Fig. 5) than that in the $PbGa_2S_4$:Nd^{3+} (0.2 molar%) crystal ($\tau = 315$ μs) (curve 6 in Fig. 5). This corresponds to the energy transfer rate of $W = 1480\ s^{-1}$. However, a contribution of concentration quenching is negligible at 0.2 molar% of Nd^{3+} and the system response is linear, due to off-resonance 1.56 μm excitation into a weak electron–phonon side-band of the $^4I_{15/2}$ level. For small concentration of Nd^{3+} a contribution of multiphonon relaxation can be calculated as the difference between the measured relaxation rate and calculated radiative relaxation rate. The calculated radiative rates of the $^4I_{15/2}$, $^4I_{13/2}$, and $^4I_{11/2}$ levels in the $PbGa_2S_4$:Nd^{3+} crystal (see Table 2) are considerably lower than the measured rates (Table 4). As a result the measured fluorescence kinetics decay is mainly determined by multiphonon relaxation. To determine the ^4I_J level with the slowest MR rate let us turn to the theory of multiphonon relaxation. According to Eqs. (1)–(6) and (9) the MR rate change for different tran-

Table 4
Measured and multiphonon relaxation decay times for Nd^{3+} nonradiatively quenched manifolds in laser crystals with low phonon spectra and parameters of nonlinear theory having influence on multiphonon transition rate

Transition	$\Delta E_{min.}$ (cm^{-1})	$\hbar\omega_{eff.} = \Delta E_{min}/p$ (cm^{-1})	Phonon number p	$(U^{(2)})^2$	$(U^{(4)})^2$	$(U^{(6)})^2$	$\tau_{meas.}/\tau_{MR}$, 14 K	τ_{meas}, 295 K
CaF_2 (pair Nd–La center) (R_0(Nd–F) = 2.36 Å)								
$^2G_{7/2} \rightarrow {}^2H_{11/2}$	1125	375	3	0.0066	0	0.3467		
$^4G_{5/2} \rightarrow {}^2H_{11/2}$				0	0.0003	0.0146	22 ns	
SrF_2 (pair Nd–La center) (R_0(Nd–F) = 2.505 Å)								
$^2G_{7/2} \rightarrow {}^2H_{11/2}$	1130		3	0.0066	0	0.3467		
$^4G_{5/2} \rightarrow {}^2H_{11/2}$		380		0	0.0003	0.0146	25 ns	
LaF_3 (R_0(Nd–F) = 2.50 Å)								
$^2G_{7/2} \rightarrow {}^2H_{11/2}$	1200		3	0.0066	0	0.0048		
$^4G_{5/2} \rightarrow {}^2H_{11/2}$		400		0	0.0003	0.0146	29 ns	15 ns
$^4G_{7/2} \rightarrow {}^4G_{5/2}$;	1546	390	4	0	0.2246	0.0503		
$^2G_{7/2}$				0.0575	0.0005	0.0377	110 ns	56 ns
$PbCl_2$ (R_0(Nd–Cl) ⩾ 2.85 Å)								
$^2G_{7/2} \rightarrow {}^2H_{11/2}$			5	0.0066	0	0.3467	18 μs/	5.5 μs/
$^4G_{5/2} \rightarrow {}^2H_{11/2}$	1000	200		0	0.0003	0.0146	54.5 μs	6.9 μs
$CaGa_2S_4$ (R_0(Nd–S) ⩾ 2.97 Å)								
$^2G_{7/2} \rightarrow {}^2H_{11/2}$	1110		3	0.0066	0	0.3467	115 ns	71 ns
$^4G_{5/2} \rightarrow {}^2H_{11/2}$		370		0	0.0003	0.0146		
$^4I_{15/2}$–$^4I_{13/2}$	1680	420–336	4–5	0.0196	0.1189	1.4511	519 μs/	278 μs/
							566 μs	291 μs
$PbGa_2S_4$ (R_0(Nd–S) ⩾ 3.12 Å)								
$^2G_{7/2} \rightarrow {}^2H_{11/2}$			3	0.0066	0	0.3467	156 ns	83 ns
$^4G_{5/2} \rightarrow {}^2H_{11/2}$	1110	370		0	0.0003	0.0146		
$^4I_{15/2}$–$^4I_{13/2}$	1680	336	5	0.0196	0.1189	1.4511	810 μs/	315 μs/
							970 μs	336 μs

sitions of a specific rare-earth ion in a specific crystal depends only on the energy gap $\Delta E = \Delta E_{min}$ to the next manifold below (the factor $\rho_p(\Delta E)$ of Eq. (9)), a degree of degeneracy of the initial level $(2J' + 1)$, and the values of the reduced matrix elements $U^{(k)}$ of the corresponding electronic transitions (Eq. (1)). For three $^4I_J - {}^4I_{J'}$ mid-IR transitions of Nd^{3+} the $U^{(k)}$ parameters are very close [15]. The largest and close values of energy gaps ΔE and, therefore, minimal values of $\rho_p(\Delta E_{J'J})$, are found for the transitions from the $^4I_{15/2}$ and $^4I_{13/2}$ manifolds (Fig. 1). Thus, the MR rates of these two levels are slower than the MR rate of the $^4I_{11/2}$ level. But the degree of the degeneracy of the $^4I_{15/2}$ level is larger than that of the low-lying $^4I_{13/2}$ level. Therefore, according to Eq. (1) the MR rate of the $^4I_{15/2}$ level should be slower and the final stage of the total ^4I_J fluorescence kinetics in $CaGa_2S_4$:Nd^{3+} and $PbGa_2S_4$:Nd^{3+} should be defined by the $^4I_{15/2}$ multiphonon relaxation rate. This argumentation is confirmed experimentally (Fig. 4).

Now, one can calculate the multiphonon relaxation rates of the $^4I_{15/2}$ level in $PbGa_2S_4$:Nd^{3+} and $CaGa_2S_4$:Nd^{3+} at different temperatures assuming that the corresponding radiative rates are independent on the temperature for both the crystals. The value of radiative rate A calculated for the $^4I_{15/2}$ level for $PbGa_2S_4$:Nd^{3+} is equal to $A = 205\ s^{-1}$. For $CaGa_2S_4$:Nd^{3+} $A = 170\ s^{-1}$ was estimated. The estimation is based on the fact that the radiative rate of the $^4F_{3/2}$ metastable level in this crystal ~1.2 times lower compared to $PbGa_2S_4$:Nd^{3+} and one may assume that the rates of the ^4I_J levels in $CaGa_2S_4$:Nd^{3+} are also ~1.2 times lower because the strongest radiative transitions from the $^4F_{3/2}$ metastable level to the $^4I_{11/2}$ and $^4I_{9/2}$ levels depend on the same matrix elements $U^{(4)}$ and $U^{(6)}$ as the transitions from the ^4I_J levels.

The $W_{MR}(T)$ temperature dependence of the $^4I_{15/2}$ manifold obtained in $PbGa_2S_4$:Nd^{3+} (Fig. 6) and $CaGa_2S_4$:Nd^{3+}

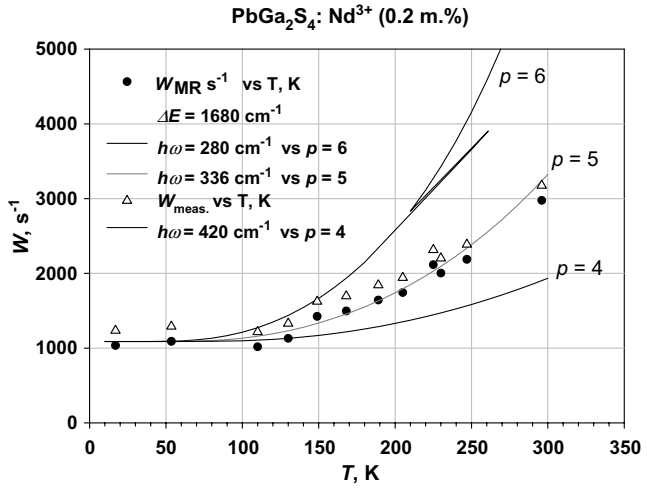

Fig. 6. Temperature dependence of the decay rate of the $^4I_{15/2}$ manifold measured at the long time scale of a sum of fluorescence kinetics of three low-lying ^4I_J manifolds of the Nd^{3+} ion and of calculated multiphonon relaxation rate ($W_{MR} = W_{meas.} - A$, $A = 200\ s^{-1}$) in the $PbGa_2S_4$:Nd^{3+} (0.2 molar%) crystal and the fitting curves for the single frequency model of crystal lattice vibrations.

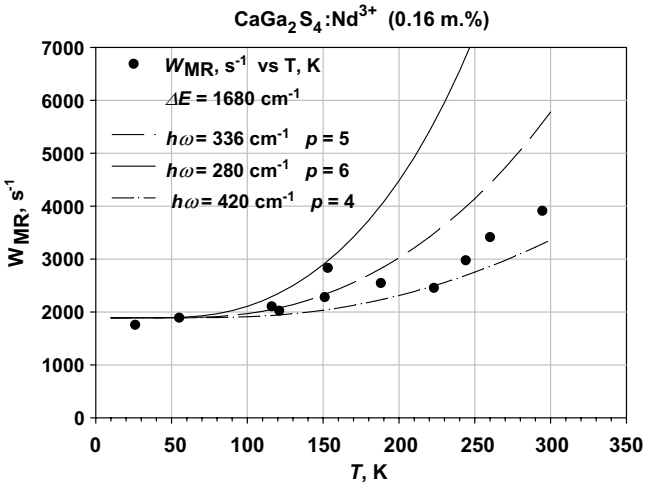

Fig. 7. Temperature dependence of the decay rate of the $^4I_{15/2}$ manifold measured at the long time scale of a sum of fluorescence kinetics of three low-lying ^4I_J manifolds of the Nd^{3+} ion and of calculated multiphonon relaxation rate ($W_{MR} = W_{meas.} - A$, $A = 170\ s^{-1}$) in the $CaGa_2S_4$:Nd^{3+} (0.16 molar%) crystal and the fitting curves for the single frequency model of crystal lattice vibrations.

(Fig. 7) is analyzed in a single-frequency model of lattice vibrations [14]. The theoretical curves of Eqs. (7) and (8) which have been drawn for the process of temperature stimulated p-phonon emission in $PbGa_2S_4$:Nd^{3+} ($p = \Delta E_{min}/\hbar\omega_2 = 1680\ cm^{-1}/420\ cm^{-1}$ – curve $p = 4$ in Fig. 6, $p = \Delta E_{min}/\hbar\omega_1 = 1680\ cm^{-1}/336\ cm^{-1}$ – curve $p = 5$ in Fig. 6, and $p = \Delta E_{min}/\hbar\omega_3 = 1680\ cm^{-1}/280\ cm^{-1}$ – curve $p = 6$ in Fig. 6) depict the boundaries of the area which covers all experimental points. It may be concluded that 5-phonon transitions have the dominant contribution to multiphonon relaxation of the $^4I_{15/2}$ manifold in $PbGa_2S_4$:Nd^{3+} crystal. For $CaGa_2S_4$:Nd^{3+} a five and four phonon transitions contributes to the $^4I_{15/2}$ relaxation rate (Fig. 7). It should be noted that dispersion of experimental points is larger for $CaGa_2S_4$:Nd^{3+} than for $PbGa_2S_4$:Nd^{3+} because of weaker fluorescence response concerned with lower concentration of Nd^{3+} in the former crystal. At low temperatures the MR rate is two times higher for the $CaGa_2S_4$:Nd^{3+} crystal than that for the $PbGa_2S_4$:Nd^{3+} one probably due to significant contribution of four phonon transitions to the MR rate. For comparison, the fluorescence kinetics decay for both the crystals at liquid helium temperatures is presented in Fig. 8.

The measured decay times of the high-lying $^4G_{5/2}$; $^2G_{7/2}$ manifold of Nd^{3+} in the $CaGa_2S_4$:Nd^{3+} (0.16 molar%) crystal in the temperature range from 13 to 300 K (Fig. 9) are practically equal to multiphonon relaxation decay times for this manifold due to the negligible contribution of radiative decay because of the nanosecond scale of multiphonon and microsecond scale of radiative relaxation (see Tables 2 and 4). The theoretical curves of Eqs. (7) and (8) which have been drawn for the processes of temperature stimulated p-phonon emission ($p = \Delta E_{min}/\hbar\omega_1 = 1110\ cm^{-1}/370\ cm^{-1}$ – solid curve $p = 3$ in Fig. 9, $p = \Delta E_{min}/\hbar\omega_2 = 1110\ cm^{-1}/280\ cm^{-1}$ – dashed curve $p = 4$ in Fig. 9) depict the boundaries of the area which covers all experimental points. It may be concluded that three phonon transitions have the dominant contribution to multiphonon relaxation of the $^4G_{5/2}$; $^2G_{7/2}$ manifold in the $CaGa_2S_4$:Nd^{3+} crystal. For the $PbGa_2S_4$:Nd^{3+} crystal the fluorescence kinetics decay for the $^4G_{5/2}$; $^2G_{7/2}$ manifold was measured at liquid helium and room temperatures, only. Again, in $PbGa_2S_4$: Nd^{3+} multiphonon relaxation is found to be slower than in $CaGa_2S_4$:Nd^{3+} (Table 4).

It is also interesting to compare the measured MR rates in Nd^{3+} doped sulfide and fluoride crystal matrixes with close values of maximum phonon frequencies to verify regularities of multiphonon relaxation predicted by the nonlinear theory. As it was stated above the multiphonon relaxation rate depends on many parameters (see equations of part 3). The dependence of the MR rate on ΔE and p

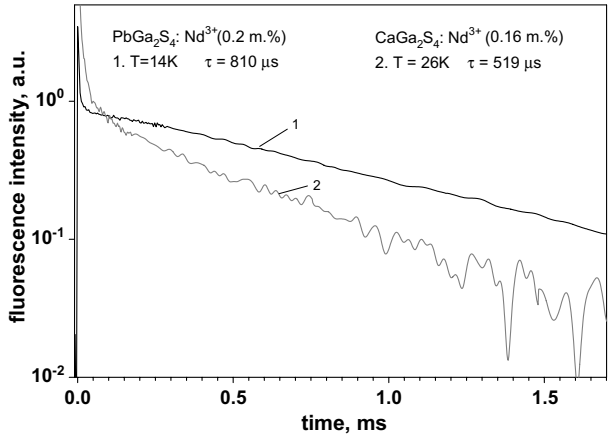

Fig. 8. A sum of fluorescence kinetics of three low-lying ^4I_J manifolds of the Nd^{3+} ion measured after 1.56 μm of laser excitation in the $PbGa_2S_4$:Nd^{3+} (0.2 molar%) (curve 1) and $CaGa_2S_4$:Nd^{3+} (0.16 molar%) (curve 2) crystals at liquid helium temperatures.

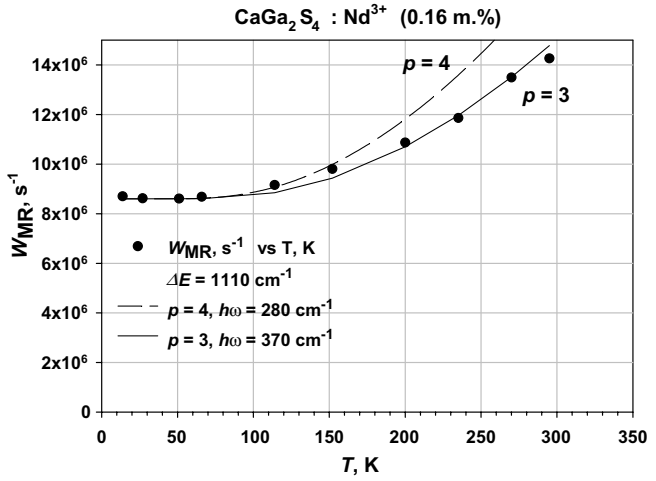

Fig. 9. Temperature dependence of the measured fluorescence kinetics decay rate of the $^4G_{5/2}$; $^2G_{7/2}$ manifold in the $CaGa_2S_4$:Nd^{3+} (0.16 molar%) crystal and the fitting curves for the single frequency model of crystal lattice vibrations.

was studied by many authors and it was established that an increase of the number of phonons p by one decreases the MR rate by one – two orders of magnitude (see Ref. [3] and the references therein). The number of phonons p is the strongest parameter and if it is fixed it is possible to find out the dependence of MR rate on other parameters, i.e. on the reduced matrix element of the unit tensor operator $U^{(k)}$ and on the rare-earth–nearest ligands distance R_0. The $U^{(k)}$ parameter can be easily fixed by taking the same transition in different crystals and then the dependence on R_0 can be analyzed. In doing so, the fluorescence decay curves of the $^4G_{5/2}$; $^2G_{7/2}$ manifolds of Nd^{3+} were measured in the CaF_2:LaF_3 (0.25%):NdF_3 (0.25%) and SrF_2:LaF_3 (1%):NdF_3 (0.2%) low phonon crystals at 14 K by direct picosecond laser excitation and resonant fluorescence detection. These crystals have close values of maximum phonon frequencies with the thiogallate crystals. Selective excitation was provided at approximately 579.45 nm wavelength directly into the Nd–La pair center (M′ center) to map out cross-relaxation quenching. Fluorescence monitoring was chosen at 657 nm in the case of SrF_2 [20] and at 653 nm in the case of CaF_2 [21,22] when the maximum of fluorescence intensity comes from the M′-center. The measured lifetimes are presented in Table 4.

The dependence of the MR rate on the RE-nearest ligands distance R_0 was firstly observed in Ref. [23] in the row of fluorite-type crystals. For example, in CdF_2:Er^{3+} ($\hbar\omega_{max} = 384\ cm^{-1}$) and SrF_2:Er^{3+} ($\hbar\omega_{max} = 383\ cm^{-1}$), the crystals with close phonon spectra, a three times increase of a decay time of the $^4I_{9/2}$ manifold from τ (CdF_2) ($R_0 = 2.34$ Å) = 14 μs to τ (SrF_2) ($R_0 = 2.505$ Å) = 50 μs was found. The measured decay times are determined by the rate of six phonon $^4I_{9/2} \rightarrow {}^4I_{11/2}$ transition ($\Delta E_{min} \approx 2180\ cm^{-1}$). The increase of a decay time of the $^4G_{5/2}$, $^2G_{7/2}$ level with an increase of Nd^{3+} to the nearest ligands distance R_0 in the row of CaF_2:Nd^{3+}, SrF_2:Nd^{3+}, LaF_3:Nd^{3+}, $CaGa_2S_4$:Nd^{3+} and $PbGa_2S_4$:Nd^{3+} crystals with close values of maximum phonon frequencies is observed now (Table 4). The measured decay times are determined by the rate of 3-phonon the $^4G_{5/2}$, $^2G_{7/2} \rightarrow {}^2H_{11/2}$ transition of Nd^{3+} ($\Delta E_{min} \approx 1100$–$1200\ cm^{-1}$). The largest R_0(Nd–S) $\geqslant$ 3.1 Å [24] in $PbGa_2S_4$:Nd^{3+} correlates with the longest measured decay time $\tau = 156$ ns in this crystal, which is 5–6 times longer than in LaF_3 ($\tau = 29$ ns) and SrF_2 ($\tau = 25$ ns), the crystals with much smaller the Nd–F distance $R_0 \approx 2.5$ Å than the Nd–S distance $R_0 \geqslant 3.1$ Å. For $CaGa_2S_4$:Nd^{3+} the distance R_0(Nd–S) $\geqslant$ 2.97 Å is in between those for $PbGa_2S_4$:Nd^{3+} and LaF_3:Nd^{3+}. And the measured decay time $\tau = 115$ ns is shorter than that in $PbGa_2S_4$:Nd^{3+} ($\tau = 156$ ns) but 3.8 times longer than in LaF_3:Nd^{3+} ($\tau = 29$ ns).

Let us address to the nonlinear theory of multiphonon relaxation to explain the measured relaxation rates $W_{MR} = 1/\tau_{MR}$ dependence on the Nd^{3+} to the nearest ligand distance R_0. In the frame of point-charge model of RE ion–ligand interaction the following equation for the MR rate of a p-phonon transition can be written (see Eqs. (1), (3) and (5))

$$W_{MR}(p) = \sum_{k=2,4,\text{ and } 6} A_{kp} R_0^{-(2k+2+2p)}, \tag{15}$$

where a factor of A_{kp} is independent on R_0, and for single-frequency model of lattice vibrations it can be expressed as

$$A_{kp} = \left(\frac{1}{137}\right)^2 \frac{cZ}{\bar{\nu}} \left(\frac{q}{e}\right)^2 \overline{\xi^k}^2 \begin{pmatrix} l & l & k \\ 0 & 0 & 0 \end{pmatrix}^2 \frac{(2l+1)^2(2p+2k)!}{(2k+1)!p!} \times \frac{(LSJ\|U^{(k)}\|L'S'J')^2}{2J'+1} \left(\frac{\hbar}{8\pi c M \bar{\nu}}\right)^p. \tag{16}$$

It was shown in Ref. [11] that in the frame of the point charge model for the transitions with a small number of phonons ($p = 3$) the main contribution to the MR rate comes from the term with $k = 2$. Besides, if one neglects the exchange-charge interaction the only term left is A_{23}. In single frequency model of lattice vibrations this parameter can be easily calculated using Eq. (16). For Nd^{3+} the mean value of the square of the radius of optical electron is equal to $\langle\xi^2\rangle = 1.01$ in units of Bohr radius [25]. The effective charge for the S^{2-} ligands is equal to $q = 2$ and that for the F^- ligands is equal to $q = 1$. For the studied crystals a number of the nearest ligands $Z = 8$. The effective phonon frequencies of the crystal lattices are presented in Table 4. The mean value of the Nd–S distance for the $CaGa_2S_4$:Nd^{3+} crystal equal to $\langle R_0\rangle = 3.02$ Å is calculated using crystallographic parameters of Ref. [24]. The parameters of $SrGa_2S_4$:Nd^{3+} are taken for $PbGa_2S_4$:Nd^{3+} and the mean value of $\langle R_0\rangle = 3.12$ Å is used for calculation of A_{23}. We suppose that in $PbGa_2S_4$:Nd^{3+} the distance is even longer than in $SrGa_2S_4$:Nd^{3+}.

Our calculation gives four times higher value of A_{23} for $CaGa_2S_4$:Nd^{3+} than that for $PbGa_2S_4$:Nd^{3+}. For the $PbGa_2S_4$:Nd^{3+} and the LaF_3:Nd^{3+} crystals the A_{23} parameters are found to be almost equal. Within this accuracy the A_{23} parameter can be considered as a constant and according to Eqs. (15) and (16) $W_{MR}(3)$ depends on R_0 as a function of R_0^{-12}. This theoretical dependence (solid curve) normalized to the measured multiphonon relaxation rate for the $PbGa_2S_4$:Nd^{3+} crystal fit rather well the measured MR rate for the $CaGa_2S_4$:Nd^{3+} crystal (Fig. 10) in spite of four times higher value of the calculated A_{23} parameter. For the LaF_3:Nd^{3+} crystal the measured MR rate is 2.6 times smaller than the predicted one in spite of equal A_{23} with $PbGa_2S_4$:Nd^{3+}. Both results may be attributed to a change of A_{kp} due to change of the $\langle\mathbf{u}^2_{cat}\rangle$ and $\langle\mathbf{u}^2_{anion}\rangle$ values in $CaGa_2S_4$:Nd^{3+} and LaF_3:Nd^{3+} comparing to $PbGa_2S_4$:Nd^{3+}, which can not be predicted by rough estimation of phonon factor η with the right part of Eq. (5) and exact expression for the phonon factor η (Eq. (4)) should be employed.

In this context the $BaIn_2S_4$:Nd^{3+} crystal with the largest Nd^{3+}–S distance ($R_0 \geqslant 3.194$ Å) and crystal structure similar to calcium and lead thiogallate crystals [24] can be proposed as a laser matrix with the reduced MR rates comparable or even slower than in $PbGa_2S_4$:Nd^{3+}.

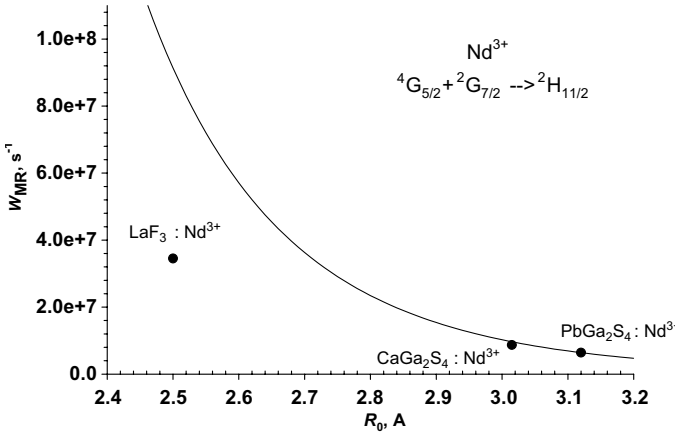

Fig. 10. The dependence of the measured multiphonon relaxation rates W_{MR} versus the distance R_0 between the Nd^{3+} ion and the nearest ligand in the $PbGa_2S_4$:Nd^{3+} (0.2 molar%), $CaGa_2S_4$:Nd^{3+} (0.16 molar%), and LaF_3:Nd^{3+} (0.5 molar%) crystals at 13 K – solid circles. Theoretical dependence of Eq. (15) for $k = 2$ and $p = 3$ (solid line) normalized to measured multiphonon relaxation rate for the $PbGa_2S_4$:Nd^{3+} crystal.

The temperature dependence of the measured decay rates of the high-lying $^4G_{5/2}$; $^2G_{7/2}$ manifold in the $PbCl_2$:Nd^{3+} (0.2 molar%) crystal in the temperature range from 13 to 300 K is presented in Fig. 11. The radiative relaxation rate was calculated from the absorption spectra using Judd–Ofelt theory. The following parameters Ω_k were found in $PbCl_2$:Nd^{3+} (0.5 molar%) ($N = 1.6 \times 10^{19}$ cm^{-3}) by a least squares method, as applied to relevant σ_{abs}^{ed} obtained from the measured absorption cross-sections $\sigma_{abs.}$ (Table 5): $\Omega_2 = 4.38 \times 10^{-20}$ cm^2, $\Omega_4 = 4.73 \times 10^{-20}$ cm^2, $\Omega_6 = 4.27 \times 10^{-20}$ cm^2. The results of calculation of radiative rates of the manifolds in this study are presented in Table 6. Calculated radiative lifetime for the $^4G_{5/2}$; $^2G_{7/2}$ manifold is $A = 37{,}200\ s^{-1}$. The measured relaxation rate at $T = 14$ K is equal to $W_{meas.} = 1/\tau_{meas.} =$

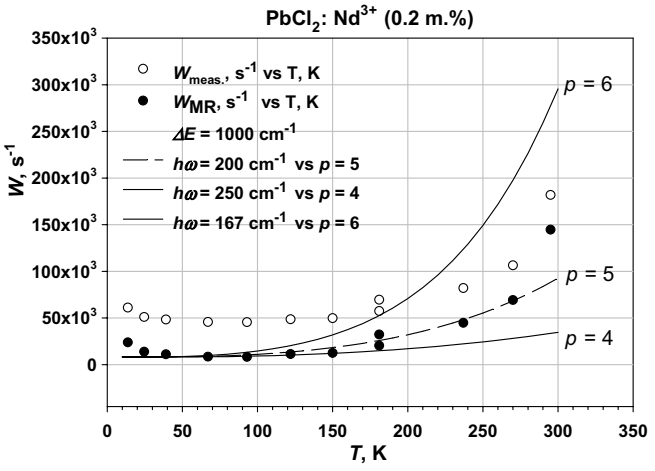

Fig. 11. Temperature dependence of the measured fluorescence kinetics decay rate and calculated multiphonon relaxation rate ($W_{MR} = W_{meas.} - A$, $A = 37{,}236\ s^{-1}$) of the $^4G_{5/2} + {}^2G_{7/2}$ manifold in the $PbCl_2$:Nd^{3+} (0.2 molar%) crystal and the fitting curves for the single frequency model of crystal lattice vibrations.

Table 5
Measured absorption cross-sections σ_{abs} in the $PbCl_2$:Nd^{3+} (0.5 molar%) crystal

Transition	σ_{abs}, 10^{-17} (cm)
$^4I_{9/2} \rightarrow {}^4F_{3/2}$	1.20
$^4I_{9/2} \rightarrow {}^4F_{5/2} + {}^2H(2)_{9/2}$	1.26
$^4I_{9/2} \rightarrow {}^4F_{7/2} + {}^4S_{3/2}$	0.54
$^4I_{9/2} \rightarrow {}^4G_{5/2} + {}^2G_{7/2}$	2.84

Table 6
Calculated radiative rates $\sum A_i$ and radiative lifetimes τ_R of the manifolds in study in the $PbCl_2$:Nd^{3+} (0.5 molar%) crystal

Manifold	A (s^{-1})	$\tau_R = 1/A$
$^4I_{11/2}$	34	29.2 ms
$^4I_{13/2}$	1090	9.2 ms
$^4I_{15/2}$	114	8.8 ms
$^4F_{3/2}$	8800	113 μs
$^4G_{5/2} + {}^2G_{7/2}$	37,200	26.9 μs
$^4G_{7/2}$	31,900	31.4 μs

54,650 s^{-1} (Table 3). So, more than half of the contribution to $^4G_{5/2}$; $^2G_{7/2}$ relaxation in the low phonon $PbCl_2$:Nd^{3+} crystal accounts for the radiative decay in spite of the small energy gap $\Delta E = 1000$ cm^{-1}. The difference between the measured and radiative rate gives the multiphonon relaxation rate. The theoretical curves of Eqs. (7) and (8), which have been drawn for the processes of temperature stimulated p-phonon emission ($p = \Delta E_{min}/\hbar\omega_1 = 1000\ cm^{-1}/250\ cm^{-1}$ – solid curve $p = 4$ in Fig. 11, $p = \Delta E_{min}/\hbar\omega_2 = 1000\ cm^{-1}/200\ cm^{-1}$ – dashed curve $p = 5$ in Fig. 11, $p = \Delta E_{min}/\hbar\omega_3 = 1000\ cm^{-1}/167\ cm^{-1}$ – solid curve $p = 6$ in Fig. 11) depict the boundaries of the area which covers all experimental points. Most of the points except room temperature lie on the theoretical curve for $p = 5$. So, it may be concluded that mainly five phonon transitions make the contribution to multiphonon relaxation of the $^4G_{5/2}$; $^2G_{7/2}$ manifold in the $PbCl_2$:Nd^{3+} crystal at $T < 270$ K. Twenty times higher the MR rate for five phonon the $^4G_{5/2}$; $^2G_{7/2} \rightarrow {}^2H_{11/2}$ transition in $PbCl_2$ Nd^{3+} ($\tau = 54.5$ μs) in comparison with the MR rate of five phonon $^4I_{15/2} \rightarrow {}^4I_{13/2}$ transition in $PbGa_2S_4$:Nd^{3+} ($\tau = 970$ μs) in spite of the lower values of $U^{(k)}$ for the former transition could be concerned with the smaller Nd–Cl distance ($R_0 \geqslant 2.85$ Å) in $PbCl_2$ [26] comparing to Nd–S distance ($R_0 \geqslant 3.1$ Å) in $PbGa_2S_4$:Nd^{3+} or underestimated radiative rate A in $PbCl_2$ Nd^{3+}. A decrease of the MR rate from 14 to 77 K (Fig. 11) may be concerned with the population of higher lying crystal field levels of the $^4G_{5/2}$; $^2G_{7/2}$ manifold. This increases the energy gap ΔE to the next manifold below and according to Eq. (9) decreases the MR rate. But above 80 K the decrease of MR rate is compensated by temperature stimulation of multiphonon relaxation (right term of Eq. (7)).

The measured inverse lifetime temperature dependence of the $^4G_{7/2}$ manifold (Fig. 12) in $PbCl_2$ Nd^{3+} is found to be completely different from the expected multiphonon relaxation $W_{MR}(T)$ temperature dependence predicted by

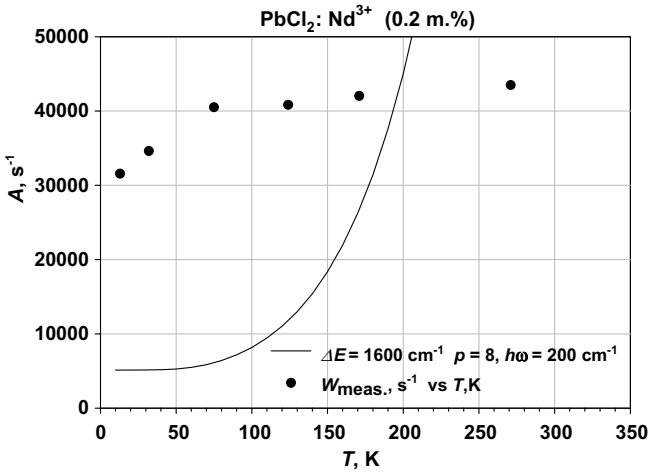

Fig. 12. Temperature dependence of the measured fluorescence kinetics decay rate of the $^4G_{7/2}$ manifold in the $PbCl_2$:Nd^{3+} (0.2 molar%) crystal and the fitting curve for the single frequency model of crystal lattice vibrations.

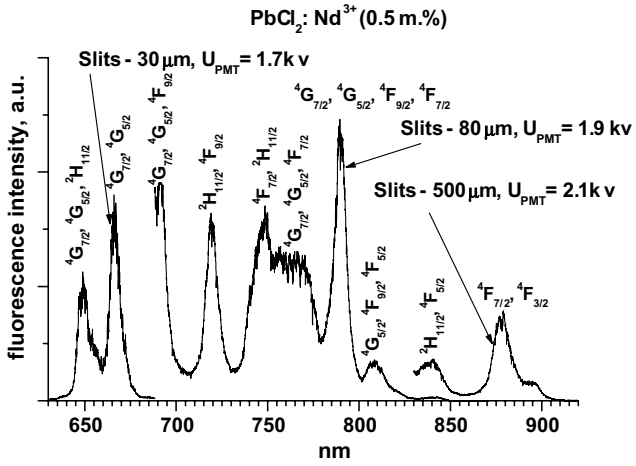

Fig. 13. The fluorescence spectra of the $PbCl_2$:Nd^{3+} (0.5 molar%) crystal in red and near IR spectral regions at room temperature measured under 532 nm second harmonics of pulsed Nd:YAG laser excitation and fluorescence monitoring using standard gated Boxcar averaging technique with one microsecond delay of time gate 250 μs long. (For interpretation of the references in colour in this figure legend, the reader is referred to the web version of this article.)

Eqs. (7) and (8) for $\Delta E_{min} \cong 1600\ cm^{-1}$, $\hbar\omega_{max} \approx 200\ cm^{-1}$ and $p = 8$. It shows that the measured fluorescence kinetics decay rate is practically constant above 80 K. The dependence is similar to that measured for the $^2F(2)_{5/2}$ high-lying Nd^{3+} manifold in $YAlO_3$:Nd^{3+} [27] and reflects the radiative nature of $^4G_{7/2}$ relaxation and its high fluorescence quantum yield in the $PbCl_2$ Nd^{3+}. The approximation used in Ref. [27] explained the measured $A(T)$ dependence by taking into consideration the difference in population n_i and radiative probabilities A_i of different crystal field levels of the studied manifold. The calculated radiative lifetime of the $^4G_{7/2}$ manifold $\tau_R = 32$ μs (Table 5) coincides with the measured decay time at 13 K (Table 3). Thus, the fluorescence related to the $^4G_{7/2}$ manifold usually strongly quenched by multiphonon relaxation in Nd^{3+} doped oxide and fluoride laser crystals is easily observed in $PbCl_2$:Nd^{3+}. In the thiogallate crystals the MR rate of the $^4G_{7/2}$ manifold is also low compared to the radiative rate. For example, the measured decay time of the $^4G_{7/2}$ manifold in $PbGa_2S_4$:Nd^{3+} (0.2 molar%) $\tau_{meas.} = 12.3$ μs at 77 K and 10.5 μs at room temperature (Table 3) is only slightly shorter than the calculated radiative decay time ($\tau_R = 13.6$ μs) (Table 2). So, the calculated fluorescence quantum yield of the $^4G_{7/2}$ manifold in $PbGa_2S_4$:Nd^{3+} is equal to 77% at room temperature.

It is very likely that other manifolds having energies in between the energies of the $^4G_{5/2}$; $^2G_{7/2}$ and $^4F_{3/2}$ manifolds are also weakly quenched by multiphonon relaxation in $PbCl_2$:Nd^{3+}. This is confirmed by the fluorescence spectra measured at room temperature in visible and near infra red spectral ranges in $PbCl_2$:Nd^{3+} (0.5 molar%) under 532 nm pulsed laser excitation. The fluorescence is measured by standard gated Boxcar averaging technique with a one microsecond delay of the time gate 250 μs long. The fluorescence spectral lines related to the $^2H_{11/2}$, $^4F_{9/2}$, $^4F_{7/2}$, $^4F_{5/2}$ manifolds is observed (Fig. 13).

The sum of kinetics of fluorescence decay of the ^4I_J manifolds and its temperature dependence were measured in the $PbCl_2$:Nd^{3+} (0.8 molar%) crystal under 1.56 μm laser excitation directly into the $^4I_{15/2}$ manifold (Fig. 14). The fluorescence intensity shows complicated temporal profile depending on temperature. At high temperatures it can be fit by double exponential decay and for temperatures lower than 190 K the temporal profile of the fluorescence kinetics decay is changed. For example, for $T = 8$ K it has twice the duration than at room temperature and exhibits long fluorescence build-up after switching off the excitation laser pulse. Full analysis of the measured fluorescence kinetics and its temperature dependence is beyond

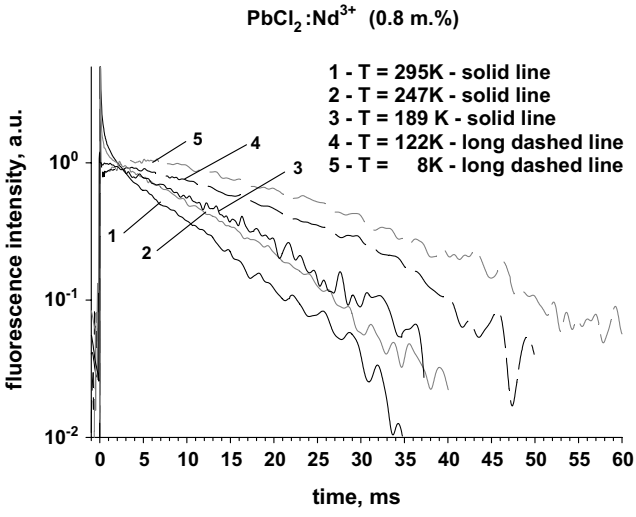

Fig. 14. Temperature dependence of integrated fluorescence kinetics of three low-lying ^4I_J manifolds in $PbCl_2$:Nd^{3+} (0.8 molar%) under 1.56 μm laser excitation and fluorescence monitoring after optical filter transparent at wavelengths longer than 3 μm.

the subject of this paper related to multiphonon relaxation and requires consideration of cross-relaxation processes. Here, we discuss only the influence of multiphonon relaxation on the fluorescence decay of the ^4I_J manifolds in $PbCl_2$:Nd^{3+}. Judd–Ofelt analysis gives the radiative decay times from approximately $\tau_R = 9$ ms for the $^4I_{15/2}$ and $^4I_{13/2}$ levels to $\tau_R = 29$ ms for the $^4I_{11/2}$ level (Table 6). The measured decay time at the long time scale of integrated fluorescence kinetics decay varies from $\tau_{meas.} = 9$ ms at room temperature to 11 ms, or may be longer, at 8 K. According to our analysis of kinetic rate equations (see Appendix) the integrated kinetics decay of the ^4I_J manifolds at the long time scale in any case is determined by the lowest relaxation rate of three ^4I_J levels. One may suppose that contribution of multiphonon relaxation is negligible for the ^4I_J manifolds in $PbCl_2$:Nd^{3+}. If that is the case then the decay time of the measured curve at the long time scale would be 29 ms. But the measured decay time is about 11 ms at low temperature. The difference related to multiphonon relaxation gives the value of the MR decay time of the $^4I_{11/2}$ level about $\tau_{MR} = 18$ ms at 8 K and fluorescence quantum yield about 38% at room temperature. This is about six times higher than for the $^4I_{15/2}$ level in $PbGa_2S_4$:Nd^{3+} ($\eta = 6.5\%$).

Low submillisecond and millisecond decay rates of fluorescence kinetics of the ^4I_J levels of Nd^{3+} in $CaGa_2S_4$, $PbGa_2S_4$, and $PbCl_2$ allows to measure and compare 4–5.5 μm fluorescence spectra at 810 nm diode laser excitation into the $^4F_{5/2}$ level at room temperature (Fig. 15). The cut-off frequency of long wavelength spectral wings for all the crystals is partially defined by the cut-off frequency of SDL spectrometer. The widest spectral range of mid-IR fluorescence (4.1–5.7 μm) is measured for the $PbGa_2S_4$:Nd^{3+} (0.2 molar%) crystal and the narrowest one (4.6–5.8 μm) for the $PbCl_2$:Nd^{3+} (0.8 molar%) crystal. In case of selective fluorescence excitation into the $^4I_{15/2}$ level the maximum of fluorescence spectral peak in the $PbGa_2S_4$ crystal shifts from 4.9 to 4.7 μm and the spectral line becomes more narrow (Fig. 16). A 4.9 μm spectral peak most likely belongs to the $^4I_{11/2} \rightarrow {}^4I_{9/2}$ transition because after laser excitation at 810 nm wavelength into the $^4F_{5/2}$ level it is rapidly relaxes to the $^4F_{3/2}$ metastable level. But the calculated branching ratio coefficient from the $^4F_{3/2}$ level to the $^4I_{11/2}$ level $\beta(^4F_{3/2} - {}^4I_{11/2}) = 0.443$ is much larger than those to the $^4I_{13/2}$ level ($\beta(^4F_{3/2} - {}^4I_{13/2}) = 0.0765$) and to the $^4I_{15/2}$ level ($\beta(^4F_{3/2} - {}^4I_{15/2}) = 0.004$). The rest of excitation goes to the background $^4I_{9/2}$ level. As a result only one excited $^4I_{11/2}$ level among the ^4I_J levels populates significantly. And in the case of direct excitation into the $^4I_{15/2}$ level the 4.7 μm fluorescence spectral peak most likely belongs to the $^4I_{15/2} \rightarrow {}^4I_{13/2}$ transition.

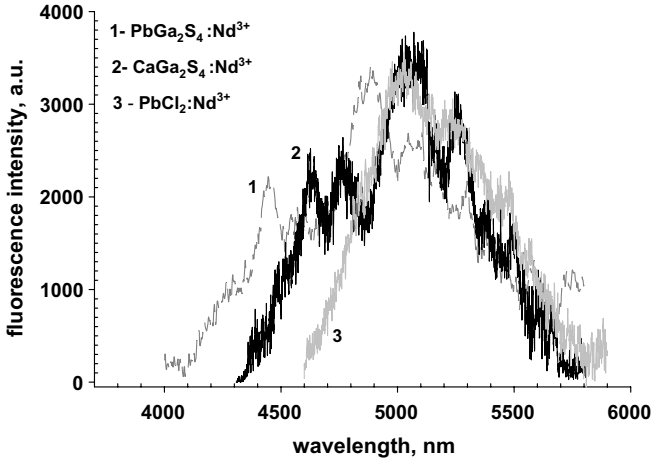

Fig. 15. Mid-IR fluorescence spectra of the $PbGa_2S_4$:Nd^{3+}, $CaGa_2S_4$:Nd^{3+}, and $PbCl_2$:Nd^{3+}crystals under CW high power (5 W) laser diode array excitation at 810 nm and fluorescence monitoring using lock-in amplifier and Ge(Au) photoresistor.

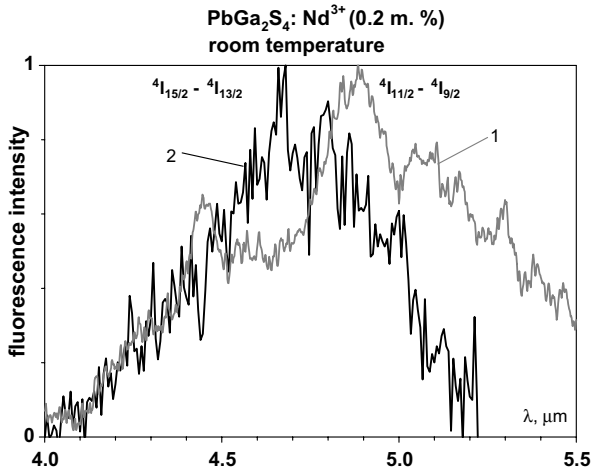

Fig. 16. A 4–5.5 μm fluorescence spectra in the $PbGa_2S_4$: Nd^{3+} (0.2 molar%) crystal for different excitation wavelengths: 810 nm – 1, 1.61 μm – 2.

5. Conclusion

Summing up, mid-IR Nd^{3+} transitions perspective for laser oscillation were analyzed in the $CaGa_2S_4$, $PbGa_2S_4$, and $PbCl_2$ crystals and compared with low phonon fluoride crystals. Fluorescence kinetics decay of the high-lying $^4G_{7/2}$ and $^4G_{5/2}$; $^2G_{7/2}$ and low-lying ^4I_J levels and its temperature dependence in the range of 13–295 K were measured. Long submillisecond and millisecond decay times of fluorescence kinetics of the ^4I_J levels of Nd^{3+} are observed and analyzed in the $CaGa_2S_4$, $PbGa_2S_4$, and $PbCl_2$ crystals. Mid-IR 4–5.5 μm fluorescence spectra of Nd^{3+} at 810 nm and 1.61 μm laser excitation wavelengths are measured in these crystals for the first time at room temperature.

For 5 μm mid-IR transitions of Nd^{3+} the radiative relaxation rates are found to be several times higher and multiphonon relaxation (MR) rates are several times lower in lead and calcium thiogallate crystals comparing to fluoride crystals with similar low phonon spectra. Large values of radiative rates in $PbGa_2S_4$:Nd^{3+}, $CaGa_2S_4$:Nd^{3+} and

$PbCl_2$:Nd^{3+} crystals are explained by large refractive indices n of a crystal host. As for multiphonon relaxation rate it is observed that, for example, in the row of the $PbGa_2S_4$:Nd^{3+}, $CaGa_2S_4$:Nd^{3+} and LaF_3:Nd^{3+} low phonon crystals the MR rate of a three phonon the $^4G_{5/2}$; $^2G_{7/2} \rightarrow {}^2H_{11/2}$ transition decreases with an increase of Nd^{3+} to the nearest ligand distance R_0. The slowest MR rates of mid-IR transitions of Nd^{3+} among the studied fluoride and sulfide crystals are found for $PbGa_2S_4$:Nd^{3+} with the largest $R_0 \geqslant 3.1$ Å. This result is in a good qualitative agreement with the nonlinear theory of multiphonon relaxation where, for example, the MR rate for p-phonon transition in the frame of point-charge model of RE and the nearest ligand interaction is equal to $W_{MR}(p) = \sum_{k=2,4,\text{ and }6} A_{kp} R_0^{-(2k+2+2p)}$, where A_{kp} is the parameter independent on R_0. This may explain the much lower MR rates in the studied sulfide crystals comparing to low phonon fluoride crystals with much smaller RE – the nearest ligand distance R_0.

The $PbCl_2$:Nd^{3+} crystal exhibits more than two orders of magnitude lower MR rates of mid-IR transitions comparing to $PbGa_2S_4$:Nd^{3+} due to much lower phonon spectrum concerned with heavier anion, but also lower radiative rates because of smaller refractive index n.

Acknowledgements

This work is partially supported by NSF grant ECS- 0140484, CRDF grant RU-E2-2585-MO-04, ISTC-EOARD grant No 2022p, and RFBR Grant No. 05-02-17447a. We would like to express our thanks to P.P. Fedorov and R.M. Zakalyukin for their help in crystal structure analysis, M.B. Johnson for the measurements of FTIR absorption spectra and E.O. Orlovskaya for her help in paper preparation.

Appendix. Kinetics of mid-IR emission

Multiphonon and radiative decay ($PbGa_2S_4$:Nd^{3+} and $CaGa_2S_4$:Nd^{3+})

$$\dot{n}_4 = -\gamma_4 n_4, \tag{A.1a}$$

$$\dot{n}_3 = -\gamma_3 n_3 + (W_{43} + V_{43}) n_4, \tag{A.1b}$$

$$\dot{n}_2 = -\gamma_2 n_2 + (W_{32} + V_{32}) n_3 + V_{42} n_4, \tag{A.1c}$$

where

$$\gamma_4 = W_{43} + V_{43} + V_{42} + V_{41}, \tag{A.2a}$$

$$\gamma_3 = W_{32} + V_{32} + V_{31}, \tag{A.2b}$$

$$\gamma_2 = W_{21} + V_{21}, \tag{A.2c}$$

W_{ij} is a probability of nonradiative transition from ith level to jth, V_{ij} is a probability of radiative transition from ith level to jth.

We neglected in Eq. (A.1) the terms of the order of W_{42}/V_{42}, W_{41}/V_{41}, and W_{31}/V_{31}, because they are well below 1. Then the values of $\tau_2 = 1/\gamma_2$, $\tau_3 = 1/\gamma_3$, and $\tau_4 = 1/\gamma_4$ can be considered as lifetimes of second, third, and fourth levels, respectively (counting from the bottom). Level one is the background level.

The solution of the set of equations (A.1) with initial conditions $n_4(0) = 1$, $n_3(0) = n_e(0) = n_1(0) = 0$ is

$$n_4(t) = n_4(0) \exp(-\gamma_4 t), \tag{A.3a}$$

$$n_3(t) = -\frac{W_{43} + V_{43}}{\gamma_4 - \gamma_3} [\exp(-\gamma_4 t) - \exp(-\gamma_3 t)] n_4(0), \tag{A.3b}$$

$$\begin{aligned} n_2(t) = {} & \frac{(W_{32} + V_{32})(W_{43} + V_{43})}{\gamma_4 - \gamma_3} \\ & \times \left[\frac{\exp(-\gamma_4 t) - \exp(-\gamma_2 t)}{\gamma_4 - \gamma_2} - \frac{\exp(-\gamma_3 t) - \exp(-\gamma_2 t)}{\gamma_3 - \gamma_2} \right] \\ & \times n_4(0) - \frac{V_{42}}{\gamma_4 - \gamma_2} [\exp(-\gamma_4 t) - \exp(-\gamma_2 t)] n_4(0) \end{aligned} \tag{A.3c}$$

Eq. (A.3a) describes exponential decay of population of the fourth (upper) level from initial value $n_4(0)$ to zero with the characteristic time $1/\gamma_4$. Eq. (A.3b) describes increasing of population of third level from initial value $n_3(0) = 0$ to a maximum value, after that the population tends to zero. In a similar way the population $n_2(t)$ varies with time.

Normalized mid-infrared intensity $I(t)/I(0)$ is equal to

$$\begin{aligned} I(t)/I(0) &= [\hbar\omega_{43} V_{43} n_4(t) + \hbar\omega_{32} V_{32} n_3(t) \\ &\quad + \hbar\omega_{21} V_{21} n_2(t)] / \hbar\omega_{43} V_{43} n_4(0) \\ &= [C_2 \exp(-\gamma_2 t) + C_3 \exp(-\gamma_3 t) + C_4 \\ &\quad \times \exp(-\gamma_4 t)] / (C_2 + C_3 + C_4). \end{aligned} \tag{A.4}$$

Here

$$C_2 = \hbar\omega_{21} V_{21} a_{22}, \tag{A.5a}$$

$$C_3 = \hbar\omega_{21} V_{21} a_{23} + \hbar\omega_{32} V_{32} a_{33}, \tag{A.5b}$$

$$C_4 = \hbar\omega_{21} V_{21} a_{24} + \hbar\omega_{32} V_{32} a_{34} + \hbar\omega_{43} V_{43} a_{44}, \tag{A.5c}$$

where

$$a_{22} = \frac{(W_{32} + V_{32})(W_{43} + V_{43})}{(\gamma_4 - \gamma_2)(\gamma_3 - \gamma_2)} + \frac{V_{42}}{\gamma_4 - \gamma_2}, \tag{A.6a}$$

$$a_{23} = -\frac{(W_{32} + V_{32})(W_{43} + V_{43})}{(\gamma_4 - \gamma_3)(\gamma_3 - \gamma_2)}, \tag{A.6b}$$

$$a_{24} = -a_{22} - a_{23}, \tag{A.6c}$$

$$a_{33} = -a_{34} = \frac{W_{43} + V_{43}}{\gamma_4 - \gamma_3}, \tag{A.6d}$$

$$a_{44} = 1. \tag{A.6e}$$

Asymptotic behavior

As it follows from Eq. (A.4), the asymptotic equation for function $I(t)/I(0)$ is

$$\lim_{t \to \infty} I(t)/I(0) \rightarrow A_k \exp(-\gamma_k t), \tag{A.7}$$

where γ_k is smallest among γ_2, γ_3, γ_4, and

$$A = C_k/(C_2 + C_3 + C_4). \tag{A.8}$$

Radiative decay ($PbCl_2$:Nd^{3+})

Let us consider the only radiative relaxation of the four-level system when radiative rates V_{ij} are much larger than nonradiative W_{ij} rates, that is

$$V_{ij} \gg W_{ij}. \tag{A.9}$$

In this case Eq. (A.1) may be simplified and rewritten Eq. (A.1) as

$$\dot{n}_4 = -\gamma_4 n_4, \tag{A.10a}$$

$$\dot{n}_3 = -\gamma_3 n_3 + V_{43} n_4, \tag{A.10b}$$

$$\dot{n}_2 = -\gamma_2 n_2 + V_{32} n_3 + V_{42} n_4, \tag{A.10c}$$

where

$$\gamma_4 = V_{43} + V_{42} + V_{41}, \tag{A.11a}$$

$$\gamma_3 = V_{32} + V_{31}, \tag{A.11b}$$

$$\gamma_2 = W_{21}. \tag{A.11c}$$

The solution of the set of equations (A.10) is

$$n_4(t) = n_4(0)\exp(-\gamma_4 t), \tag{A.12a}$$

$$n_3(t) = -\frac{V_{43}}{\gamma_4 - \gamma_3}[\exp(-\gamma_4 t) - \exp(-\gamma_3 t)]n_4(0), \tag{A.12b}$$

$$n_2(t) = \frac{V_{32}V_{43}}{\gamma_4 - \gamma_3}\left[\frac{\exp(-\gamma_4 t) - \exp(-\gamma_2 t)}{\gamma_4 - \gamma_2} - \frac{\exp(-\gamma_3 t) - \exp(-\gamma_2 t)}{\gamma_3 - \gamma_2}\right] \times n_4(0) - \frac{V_{42}}{\gamma_4 - \gamma_2}[\exp(-\gamma_4 t) - \exp(-\gamma_2 t)]n_4(0). \tag{A.12c}$$

In considered case the normalized infrared intensity $I(t)/I(0)$ has the same form as Eq. (A.4)

$$\begin{aligned} I(t)/I(0) &= [\hbar\omega_{43}V_{43}n_4(t) + \hbar\omega_{32}V_{32}n_3(t) \\ &\quad + \hbar\omega_{21}V_{21}n_2(t)]/\hbar\omega_{43}V_{43}n_4(0) \\ &= [C_2\exp(-\gamma_2 t) + C_3\exp(-\gamma_3 t) + C_4 \\ &\quad \times \exp(-\gamma_4 t)]/(C_2 + C_3 + C_4), \end{aligned} \tag{A.13}$$

with the same form of coefficients C_k

$$C_2 = \hbar\omega_{21}V_{21}a_{22}, \tag{A.14a}$$

$$C_3 = \hbar\omega_{21}V_{21}a_{23} + \hbar\omega_{32}V_{32}a_{33}, \tag{A.14b}$$

$$C_4 = \hbar\omega_{21}V_{21}a_{24} + \hbar\omega_{32}V_{32}a_{34} + \hbar\omega_{43}V_{43}a_{44}. \tag{A.14c}$$

However, coefficients a_{ik} in Eqs. (A.14) are equal now to

$$a_{22} = \frac{V_{32}V_{43}}{(\gamma_4 - \gamma_2)(\gamma_3 - \gamma_2)} + \frac{V_{42}}{\gamma_4 - \gamma_2}, \tag{A.15a}$$

$$a_{23} = -\frac{V_{32}V_{43}}{(\gamma_4 - \gamma_3)(\gamma_3 - \gamma_2)}, \tag{A.15b}$$

$$a_{24} = -a_{22} - a_{23}, \tag{A.15c}$$

$$a_{33} = -a_{34} = \frac{V_{43}}{\gamma_4 - \gamma_3}, \tag{A.15d}$$

$$a_{44} = 1. \tag{A.15e}$$

Asymptotic behavior of radiative decay

As is it follows from Eq. (A.13), the asymptotic equation for $I(t)/I(0)$ function again has a form:

$$\lim_{t\to\infty} I(t)/I(0) \to B_k\exp(-t/\tau_k), \tag{A.16}$$

where $\tau_k = 1/\gamma_k$ is the longest lifetime among $\tau_2 = 1/\gamma_2$, $\tau_3 = 1/\gamma_3$, $\tau_4 = 1/\gamma_4$ lifetimes, and

$$B_k = C_k/(C_2 + C_3 + C_4). \tag{A.17}$$

References

[1] S.R. Bowman, L.B. Shaw, B.J. Feldman, J. Ganem, IEEE J. Quantum Electron. 32 (1996) 646.
[2] S.R. Bowman, S.K. Searles, N.W. Jenkins, S.B. Qadri, E.F. Skelton, J. Ganem, in: Proceedings of Advanced Solid State Lasers Conference, Seattle, Washington, 2001, p. 84.
[3] Yu.V. Orlovskii, K.K. Pukhov, T.T. Basiev, T. Tsuboi, Opt. Mater. 4 (1995) 583.
[4] M.C. Nostarnd, R.H. Page, S.A. Payne, W.F. Krupke, Opt. Lett. 24 (1999) 1215.
[5] T.T. Basiev, M.E. Doroshenko, V.V. Osiko, V.V. Badikov, in: Advanced Solid State Photonics, February 6–8, 2005, Vienna, Austria, Technical digest, TuB10.
[6] Laser Materials and Technologies Research Center of General Physics Institute RAS, Final report, Contract no. EOARD F61775-99- WE033, 2000.
[7] J.P. Hurrel, V.J. Minkiewicz, Solid State Commun. 8 (1970) 463.
[8] Yu.V. Orlovskii, T.T. Basiev, K.K. Pukhov, N.A. Glushkov, O.K. Alimov, S.B. Mirov, in: Gregory Quarles (Ed.), The Proceedings Volume of the Advanced Solid-State Photonics 2004, TOPS, vol. 94, Optical Society of America, Washington, DC, 2004, p. 440.
[9] K.K. Pukhov, V.P. Sakun, Phys. Stat. Sol.(b) 95 (1979) 391.
[10] K.K. Pukhov, Fiz. Tverd. Tela 31 (1989) 144 [Sov. Phys. Solid State, 31 (1989) 1557].
[11] Yu.V. Orlovskii, R.J. Reeves, R.C. Powell, T.T. Basiev, K.K. Pukhov, Phys. Rev. B 49 (1994) 3821.
[12] T.T. Basiev, Yu.V. Orlovskii, K.K. Pukhov, V.B. Sigachev, M.E. Doroshenko, I.N. Vorob'ev, J. Lumin. 68 (1996) 241.
[13] T.T. Basiev, Yu.V. Orlovskii, K.K. Pukhov, F. Auzel, Laser Phys. 7 (1997) 1139.
[14] L.A. Riseberg, H.W. Moos, Phys. Rev. 174 (1968) 429.
[15] W.T. Carnall, Hannah Crosswhite, H.M. Crosswhite, Aragone National Laboratory, Internal Report, 1977.
[16] B.R. Judd, Phys. Rev. 127 (1962) 750.
[17] G.S. Ofelt, J. Chem. Phys. 37 (3) (1962) 511.
[18] M.J. Weber, Phys. Rev. 157 (1967) 262.
[19] A.A. Kornienko, personal communication.
[20] Yu.V. Orlovskii, T.T. Basiev, I.N. Vorob'ev, V.V. Osiko, A.G. Papashvili, A.M. Prokhorov, Laser Phys. 6 (1996) 448.
[21] Yu.V. Orlovskii, T.T. Basiev, S.A. Abalakin, I.N. Vorob'ev, O.K. Alimov, A.G. Papashvili, K.K. Pukhov, J. Lumin. 76–77 (1998) 371.
[22] Yu.V. Orlovskii, T.T. Basiev, A.G. Papashvili, I.N. Vorob'ev, O.K. Alimov, V.V. Osiko, J. Heber, J. Lumin. 99 (3) (2002) 233.
[23] Yu.V. Orlovskii, T.T. Basiev, K.K. Pukhov, I.N. Vorob'ev, A.G. Papashvili, F. Pelle, V.V. Osiko, J. Lumin. 94–95 (2001) 791.
[24] B. Eisenmann, M. Jakowski, W. Klee, H. Schafer, Rev. Chimie Minerale 20 (1983) 255.
[25] A. Abraham, B. Bleany, Paramagnetic Resonance of Transition Ions, Claredon Press, Oxford, 1970.
[26] K. Nitsch, M. Dusek, M. Nikl, K. Polak, M. Rodova, Prog. Crystal Growth Charact. 30 (1995) 1.
[27] T.T. Basiev, A. Yu. Dergachev, Yu. V. Orlovskii, A.M. Prokhorov, in: Proceedings of General Physics Institute, vol. 46, Moscow, Nauka, 1994, p. 3.